Received 13 December 2021; revised 19 January 2022; accepted 23 January 2022. Date of publication 28 January 2022; date of current version 4 February 2022.

Digital Object Identifier 10.1109/OJAP.2022.3147015

Statistics of the Effective Massive MIMO Channel in Correlated Rician Fading

JENS ABRAHAM [1] (Graduate Student Member, IEEE), PABLO RAMÍREZ-ESPINOSA [2], AND TORBJÖRN EKMAN [1] (Member, IEEE)

[1] Department of Electronic Systems, Norwegian University of Science and Technology, 7491 Trondheim, Norway

[2] Department of Electronic Systems, Connectivity Section, Aalborg University, 9220 Aalborg, Denmark

CORRESPONDING AUTHOR: J. ABRAHAM (e-mail: jens.abraham@ntnu.no)

ABSTRACT Massive multiple-input multiple-output base stations use multiple spatial diversity branches, which are often assumed to be uncorrelated in theoretical work. Correlated branches are seldom considered since they are mathematically less tractable. For correlated Rician fading, only the first- and second-order moments have been explored. To describe propagation environments more accurately, full distribution functions are needed. This manuscript provides distribution functions for the maximum ratio combining effective channel, a quadratic form of a random complex normal channel vector. Its mean vector and covariance matrix are based on a plane wave model incorporating array geometry, antenna element pattern, power angular spectra and power delay profiles. Closed-form approximations of the distribution functions are presented, to allow the fast evaluation of many real-world scenarios. The statistical framework is used to show that low-directivity antenna elements provide better performance in angular constricted Rician fading with off-axis incidence than high-directivity elements. Moreover, two base station array layouts are compared, showing that a half-circle array illuminates a cell more evenly than a uniform linear array. With the full distribution functions available, performance can be compared over the full range of received powers and not only based on the average signal-to-noise ratio.

INDEX TERMS Antenna arrays, diversity, probability density function, Rician channels, spatial correlation.

I. INTRODUCTION

IN MANY massive multiple-input multiple-output (MIMO) systems, users are communicating over multiple sub-carriers with a base station (BS) equipped with a large-scale antenna system (LSAS). These systems provide not only better performance for conventional cellular networks [1], but have benefits in Internet of Things applications too [2], [3]. Time division duplex transmission is necessary, if channel reciprocity should allow for simplified channel state information acquisition. On one hand, the radio channel is often modeled with uncorrelated antennas subject to narrow-band Rayleigh or Rician fading. On the other hand, measurement campaigns provide evidence that the radio channel is correlated in space, time and frequency. For massive MIMO systems, correlated Rician fading has been considered in context of the spectral efficiency [4] and cell-free systems [5], [6]. Those contexts only evaluate the first- and/or second-order behaviour of correlated narrow-band Rician fading channels.

To fully cover wide-band correlated Rician fading in LSAS, this work describes a complex normal random vector ($\mathcal{CN}$-RV) model with a non-trivial covariance matrix. The vector elements are representing channel coefficients for antennas and delay taps, to allow the joint consideration of the spatial and the delay domain. The covariance matrix allows to model correlation between antenna elements for the same delay tap, different delay taps of the same antenna element and mixtures where necessary. The spatial domain is parameterised by antenna element positions and corresponding power angular spectrums (PASs), whilst the delay domain is covered by power delay profiles (PDPs). The model allows to consider correlation between antennas as well as delay taps. Hence it incorporates aspects needed to derive a physically motivated distribution

for the effective channel power gain arising from maximum ratio combining (MRC). To that extent, the influence of incidence of a deterministic channel component,[1] its magnitude and correlation of the diffuse channel on single user performance is presented. We provide (accurate approximate) probability density functions (PDFs) and cumulative distribution functions (CDFs) for the effective channel gain. Moreover, the steepness of the effective channel CDF is evaluated to investigate the local diversity [7] in closed-form for different outage probabilities.

Related to this work is the effective channel with selection combining for several equally correlated fading distributions given in [8]. The capacity for correlated Rayleigh MIMO channels has been derived by characterizing distributions of eigenvalues of the propagation environment [9]. For correlated Rician channels, the eigenvalue spread of the covariance matrix and the angle of the deterministic component vector with respect to the range space of the covariance matrix are key quantities of performance metrics in [10]. Furthermore, they provide a power and a Laguerre series expansion of the effective channel. Another power series approximation of the narrow-band MRC effective channel signal to noise ratio for antennas in a linear array is given in [11]. The ergodic capacity of MRC for correlated Rician channels has been evaluated in [12], showing that a correlated Rician fading channel can improve over an uncorrelated channel under very specific circumstances. For uncorrelated Rician fading, massive MIMO systems have been analyzed based on asymptotic expressions for the signal to interference plus noise ratio in a multi-cell system [13]. For correlated Rician fading of a multi-cell massive MIMO scenario, different channel estimators and their resulting $\mathcal{CN}$-RV parameters have been derived in [4]. Channel hardening and spectral efficiency in correlated Rician fading for cell-free massive MIMO has been discussed in [5], [6]. A more generalized complex normal channel has been considering a Weichselberger correlation model and was analyzed with focus on channel hardening and favorable propagation [14]. We observe, that the full statistics of correlated Rician fading channels for LSAS have not been presented so far, since they go beyond the first- and second-order statistic of the effective channel gain.

Other correlation matrix models than the Weichselberger model have been proposed in the literature. A *constant correlation matrix*, where each pair of antennas is equally correlated [15], provides a simplistic approximation. An *exponential correlation matrix*, where the difference of antenna indices determines the correlation coefficient [16], is a more realistic approximation for uniform linear arrays (ULAs). A *generalized correlation matrix* model, where the correlation coefficient is a function of the Euclidean distance between antenna elements, has been recently discussed in [17] and can provide approximations for more general array configurations like an uniform rectangular array. A more propagation motivated *3D local scattering model* with arbitrary geometry, considering the position of array elements and the angle of arrival distribution of the diffuse radio channel, has been presented [18, Sec. 7.3.2].

In this work, we add antenna element pattern explicitly to the 3D local scattering model, to analyse the effect of low or high directivity elements, that not necessarily point into the same direction. The result is a physically meaningful parametrization of the correlation matrix elements, whereas the aforementioned general Weichselberger model has a higher abstraction level based on eigenvalues and eigenbases. Moreover, this manuscript extends our work on the effective channel in uncorrelated Rayleigh fading [19]. *Our main contribution is a method to obtain the statistics of the effective massive MIMO channel in correlated Rician fading.* This is achieved by describing a wide-band massive MIMO system as a non-central $\mathcal{CN}$-RV (Section II). The effective channel gain is a complex Gaussian quadratic form (CGQF) for which an improved accurate approximation of the PDF and CDF is provided via a confluent CGQF (Section III). To utilize the $\mathcal{CN}$-RV model, mean and covariance are characterized considering physical properties of the propagation environment (Section IV):

- a 3D local scattering model under consideration of PASs,
- antenna pattern of arbitrarily positioned and oriented BS array elements and
- PDPs with Rician fading taps.

The findings are used to compare BSs with a ULA or a half circle array for antenna elements with varying directivity after verification of the CGQF method with simulations (Section V).

The manuscript is structured as follows: it introduces the correlated complex normal channel in Section II; provides the distribution functions of the effective channel gain in Section III; shows some examples for the spatial correlation in Section IV; continues with simulations for different scenarios in Section V and closes with discussion and conclusion in Section VI and Section VII, respectively.

A. NOTATION

A variable is represented as a scalar a, a vector $\boldsymbol{a}$ or a matrix $\mathbf{A}$. Square brackets are picking an element from a structure according to the subscript, e.g., $[\boldsymbol{a}]_i$ is the i-th element of vector $\boldsymbol{a}$. The transpose and hermitian operator are $(\cdot)^{\mathrm{T}}$ and $(\cdot)^{\mathrm{H}}$. The expectation and variance of random variables are denoted with $\mathbb{E}\{\cdot\}$ and $\mathbb{V}\{\cdot\}$, respectively. The symbols $\mathcal{CN}$, χ^2 and χ'^2 designate the complex normal, central χ-squared and non-central χ-squared distribution, where, e.g., $a \sim \mathcal{CN}(0,1)$ means that a is distributed according to a central standard complex normal distribution. The angles of the spherical coordinate system are θ for the azimuth ($\theta \in [0, 2\pi]$) and ϕ the polar angle ($\phi \in [0, \pi]$).

1. The deterministic channel component can originate from a line of sight component or a specular component.

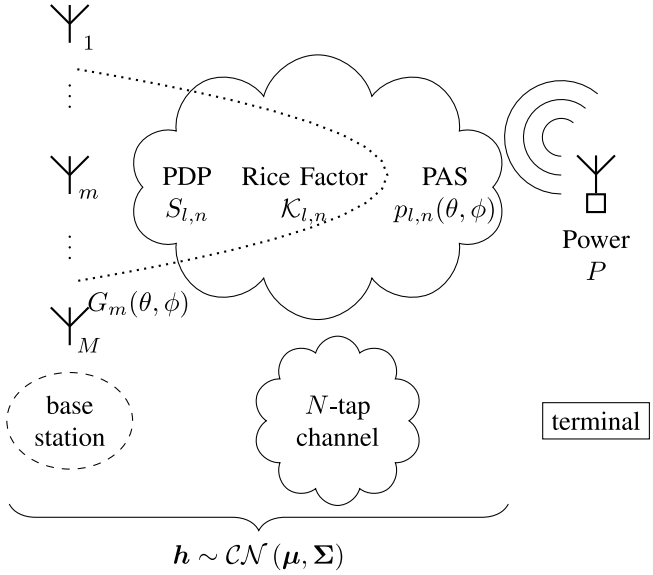

FIGURE 1. The complex normal random vector channel parameters $\mu \in \mathbb{C}^{MN}$ and $\Sigma \in \mathbb{C}^{MN \times MN}$ are determined by the M antenna elements (with individual antenna element pattern $G_m(\theta, \phi)$) and physical properties of delay taps n (power delay profile (PDP) $S_{l,n}$, Rice Factor $\mathcal{K}_{l,n}$ and power angular spectrum (PAS) $p_{l,n}(\theta, \phi)$) of the propagation environment for antennas in potentially different local areas l.

II. CORRELATED COMPLEX NORMAL CHANNEL

In this section, a correlated $\mathcal{CN}$-RV $\boldsymbol{h} \in \mathbb{C}^{MN} \sim \mathcal{CN}(\boldsymbol{\mu}, \boldsymbol{\Sigma})$ is introduced to model the end-to-end propagation between a user terminal and a BS with M antenna elements observing a N-tap channel. We are going to describe the mean vector $\boldsymbol{\mu} \in \mathbb{C}^{MN}$ and covariance matrix $\boldsymbol{\Sigma} \in \mathbb{C}^{MN \times MN}$ based on antenna element locations $\boldsymbol{r}_m$ and pattern $G_m(\theta, \phi)$ for antenna element m in conjunction with the PASs $p_{l,n}(\theta, \phi)$,[2] PDPs $S_{l,n}$ and Rician $\mathcal{K}$-factors $\mathcal{K}_{l,n}$ of the propagation environment. The index l describes a subarray which belongs to a local area where the statistics are stationary during tap n and the propagation environment is illuminated by a terminal with power P. An overview of all constituents of the model is given in Fig. 1. This model describes directly the observable channel coefficients and received powers at the BS elements and highlights the impact of BS array design on the effective channel gain.

A. PROPAGATION ENVIRONMENT

The antenna element m, local area l and delay tap n will be omitted for ease of notation in the following subsections unless they are necessary to distinguish between quantities.

The PDP coefficient S describes the user transmit power that is spread into a delay tap. The corresponding Rician factor $\mathcal{K}$ further defines the quotient between the deterministic component $\bar{h}$ and the diffuse component $\tilde{h}$ of that delay tap.

The PAS $p(\theta, \phi)$ is split into parts too, to represent the deterministic component with the incidence angles $\bar{\theta}$ and $\bar{\phi}$ as

$$\bar{p}(\theta, \phi) = \delta\big(\theta - \bar{\theta}\big)\delta\big(\phi - \bar{\phi}\big) \tag{1}$$

2. The term PAS is used here for both the PAS and the PDF of the PAS, because the PDP absorbs the power scaling.

and $\tilde{p}(\theta, \phi)$ absorbing the diffuse component. Both, $\bar{p}(\theta, \phi)$ and $\tilde{p}(\theta, \phi)$ are a PDF. The PAS under consideration of the $\mathcal{K}$-factor can now be described by

$$p(\theta, \phi) = \frac{\mathcal{K}\bar{p}(\theta, \phi) + \tilde{p}(\theta, \phi)}{\mathcal{K} + 1}. \tag{2}$$

B. CHANNEL REALIZATIONS

A Rician channel coefficient h can be composed by superposition of a plane wave for the deterministic component $\bar{h}$ and a large number of Z plane waves distributed according to the PAS to represent the diffuse component $\tilde{h}$:

$$h = \bar{h} + \tilde{h}. \tag{3}$$

The wavevector $\boldsymbol{k}$ of a wave with incidence angles θ and ϕ at wavelength λ is given by

$$\boldsymbol{k}(\theta, \phi) = \frac{2\pi}{\lambda}\begin{bmatrix}\cos\theta \sin\phi \\ \sin\theta \sin\phi \\ \cos\phi\end{bmatrix}. \tag{4}$$

This wave has phase φ at position $\boldsymbol{r}$:

$$\varphi(\theta, \phi) = \boldsymbol{k}(\theta, \phi) \cdot \boldsymbol{r}. \tag{5}$$

The deterministic component $\bar{h}$ is given by the PDP coefficient S, the Rician $\mathcal{K}$-factor $\mathcal{K}$, the antenna element pattern $G(\theta, \phi)$ and the phase term:

$$\bar{h} = \sqrt{S\frac{\mathcal{K}}{\mathcal{K}+1}G(\bar{\theta}, \bar{\phi})}\exp\big(\mathrm{j}\bar{\varphi}(\bar{\theta}, \bar{\phi})\big). \tag{6}$$

The diffuse component $\tilde{h}$ is composed with a sum over N plane waves:

$$\tilde{h} = \sqrt{\frac{S}{\mathcal{K}+1}}\sqrt{\frac{1}{N}}\sum_{z=1}^{Z}\sqrt{G\Big(\tilde{\theta}_n, \tilde{\phi}_n\Big)}a_z \exp\Big(\mathrm{j}\tilde{\varphi}_z\Big(\tilde{\theta}_n, \tilde{\phi}_n\Big)\Big) \tag{7}$$

with a_z being independent identically distributed (iid) random magnitudes, drawn from a central standard complex normal distribution. The exponential term describes the additional phase of the incoming plane wave n due to antenna element position $\boldsymbol{r}$ for an incidence wave vector $\boldsymbol{k}_z$.

C. MEAN AND AUTO-COVARIANCE

The channel realizations for all M antennas and all N taps are conditioned on the propagation environment and antenna array properties as described for the individual coefficient in (6) and (7). To capture the mean and covariance of the correlated random vector, explicit mappings of indices i and j to antenna elements m_i, m_j and delay taps n_i and n_j are necessary. The mapping follows

$$i = m_i + (n_i - 1)M \tag{8}$$

$$j = m_j + \big(n_j - 1\big)M \tag{9}$$

to consecutively identify each antenna-tap pair uniquely. Antenna elements m_i and m_j belong to the local areas l_i and l_j, respectively.

The mean vector element $[\boldsymbol{\mu}]_i$ is simply the realization in (6) because all variables are deterministic:

$$[\boldsymbol{\mu}]_i = \mathbb{E}\{h_{m_i,n_i}\} = \bar{h}_{m_i,n_i}. \tag{10}$$

The main diagonal of the covariance matrix $\boldsymbol{\Sigma}$ consists of auto-covariances of the realizations of the diffuse component in (7):

$$\begin{aligned}[\boldsymbol{\Sigma}]_{i,i} &= \mathbb{V}\{h_{m_i,n_i}\} = \mathbb{E}\left\{\tilde{h}_{m_i,n_i}\tilde{h}^{\star}_{m_i,n_i}\right\} \\ &= \frac{S}{\mathcal{K}+1}\iint_{\Omega}|G(\theta,\phi)|\tilde{p}(\theta,\phi)d\Omega. \end{aligned}\tag{11}$$

The second line of the last equation is a consequence for $Z \to \infty$ and replacement of the sum by integration over the full sphere surface Ω to account for all directions of incident waves. Here, the pattern of antenna element m_i is weighting the PAS.

D. CROSS-COVARIANCES AND CORRELATIONS

The remaining entries of the covariance matrix depend on the correlation coefficient $\rho_{i,j}$ between pairs of antennas and taps:

$$[\boldsymbol{\Sigma}]_{i,j} = \rho_{i,j}\sqrt{[\boldsymbol{\Sigma}]_{i,i}[\boldsymbol{\Sigma}]_{j,j}}. \tag{12}$$

The correlation coefficient $\rho_{i,j}$ is by definition:

$$\rho_{i,j} = \frac{\mathbb{E}\left\{\tilde{h}_{m_i,n_i}\tilde{h}^{\star}_{m_j,n_j}\right\}}{\sqrt{\mathbb{E}\left\{\tilde{h}_{m_i,n_i}\tilde{h}^{\star}_{m_i,n_i}\right\}\mathbb{E}\left\{\tilde{h}_{m_j,n_j}\tilde{h}^{\star}_{m_j,n_j}\right\}}}, \tag{13}$$

where only diffuse components have an influence on the covariance matrix $\boldsymbol{\Sigma}$. In the following, we will restrict our focus to radio channels exhibiting *uncorrelated scattering* in the same local area ($l_i = l_j = l$)

$$\rho_{i,j} = \rho^{t}_{m_i,m_j}\delta(l_i - l_j)\delta(n_i - n_j), \tag{14}$$

because our interest is focused on the influence of antenna element correlations. The correlated scattering case is left for future investigation. It might arise from antenna elements being spaced so far from each other, that the same scatterer influences different delay taps of those elements. The restriction here imposes a diagonal block structure on the covariance matrix $\boldsymbol{\Sigma}$, where each block $\boldsymbol{\Sigma}^t$ describes the correlation between antenna elements for tap t.

The antenna correlation coefficient $\rho^{t}_{m_i,m_j}$ is shown in (16), shown at the bottom of the page, and is an extension of the 3D local scattering model [18, Sec. 7.3.2] due to the consideration of antenna element pattern. The local scattering model has an impact on the handling of correlation between antennas in different local areas. We are assuming that the local areas are distant enough, such that the incoming plane waves are decorrelated. Each incident plane wave in local area l produces a direction dependent phase shift $\Delta\varphi_{m_i,m_j}$ between antenna elements at positions $\boldsymbol{r}_{m_i}$ and $\boldsymbol{r}_{m_j}$:

$$\Delta\varphi_{m_i,m_j}(\theta,\phi) = \boldsymbol{k}(\theta,\phi)\cdot\left(\boldsymbol{r}_{m_i} - \boldsymbol{r}_{m_j}\right). \tag{15}$$

The expectation over the sum of plane waves in (16) is replaced for $Z \to \infty$ by an integration over the full sphere Ω in (17), shown at the bottom of the page. The diffuse PASs $\tilde{p}_{l,t}(\theta,\phi)$ conditions the incident plane waves and the integral incorporates antenna positions as well as antenna element pattern. This allows to determine the missing elements of the correlation matrix $\boldsymbol{\Sigma}$ required for a full characterization of the $\mathcal{CN}$-RV $\boldsymbol{h}$.

E. SUMMARY

The $\mathcal{CN}$-RV $\boldsymbol{h} \sim \mathcal{CN}(\boldsymbol{\mu}, \boldsymbol{\Sigma})$ is fully characterized based on antenna positions, antenna pattern, PDPs, Rician $\mathcal{K}$-factors, PASs. The dependencies of elements of the mean vector and the covariance matrix are summarized in the following lines, where antenna elements, delay taps and local areas are explicitly designated in the subscripts of the variables:

$$[\boldsymbol{\mu}]_i \leftarrow S_{m_i,n_i}, \mathcal{K}_{m_i,n_i}, G_{m_i}(\theta,\phi), \bar{p}_{l_i,n_i}(\theta,\phi), \boldsymbol{r}_{m_i}, \lambda \tag{18}$$

$$[\boldsymbol{\Sigma}]_{i,i} \leftarrow S_{m_i,n_i}, \mathcal{K}_{m_i,n_i}, G_{m_i}(\theta,\phi), \tilde{p}_{l_i,n_i}(\theta,\phi) \tag{19}$$

$$\rho_{i,j} \leftarrow G_{m_i}(\theta,\phi), G_{m_j}(\theta,\phi), \tilde{p}_{l_i,n_i}(\theta,\phi), \tilde{p}_{l_j,n_j}(\theta,\phi), \left(\boldsymbol{r}_{m_i} - \boldsymbol{r}_{m_j}\right), \lambda \tag{20}$$

$$[\boldsymbol{\Sigma}]_{i,j} \leftarrow S_{m_i,n_i}, S_{m_j,n_j}, \mathcal{K}_{m_i,n_i}, \mathcal{K}_{m_j,n_j}, G_{m_i}(\theta,\phi), G_{m_j}(\theta,\phi), \tilde{p}_{l_i,n_i}(\theta,\phi), \tilde{p}_{l_j,n_j}(\theta,\phi), \left(\boldsymbol{r}_{m_i} - \boldsymbol{r}_{m_j}\right), \lambda \tag{21}$$

The channel vector can be reshaped into a $M \times N$ matrix and multiplication of a discrete Fourier transform matrix from the right allows a transformation into the frequency domain if needed. That common matrix form of the channel in both delay and frequency domain does not allow to keep the individual correlations between pairs of antennas and taps separate. The covariance matrix $\boldsymbol{\Sigma}$ of the $\mathcal{CN}$-RV

$$\rho^{n}_{m_i,m_j} = \frac{\mathbb{E}_{\tilde{\theta}_z,\tilde{\phi}_z}\left\{\sum_{z=1}^{Z}\sqrt{G_{m_i}\left(\tilde{\theta}_z,\tilde{\phi}_z\right)}\sqrt{G_{m_j}\left(\tilde{\theta}_z,\tilde{\phi}_z\right)}^{\star}\exp\left(\mathrm{j}\left(\tilde{\varphi}_{z,m_i}\left(\tilde{\theta}_z,\tilde{\phi}_z\right) - \tilde{\varphi}_{z,m_j}\left(\tilde{\theta}_z,\tilde{\phi}_z\right)\right)\right)\right\}}{\sqrt{\mathbb{E}_{\tilde{\theta}_z,\tilde{\phi}_z}\left\{\sum_{z=1}^{Z}\left|G_{m_i}\left(\tilde{\theta}_z,\tilde{\phi}_z\right)\right|\right\}\mathbb{E}_{\tilde{\theta}_z,\tilde{\phi}_z}\left\{\sum_{z=1}^{Z}\left|G_{m_j}\left(\tilde{\theta}_z,\tilde{\phi}_z\right)\right|\right\}}} \tag{16}$$

$$\rho^{n}_{m_i,m_j} = \frac{\iint_{\Omega}\tilde{p}_{l,n}(\theta,\phi)\sqrt{G_{m_i}(\theta,\phi)}\sqrt{G_{m_j}(\theta,\phi)}^{\star}\exp\left(\mathrm{j}\Delta\varphi_{m_i,m_j}(\theta,\phi)\right)d\Omega}{\sqrt{\iint_{\Omega}\tilde{p}_{l,n}(\theta,\phi)\left|G_{m_i}(\theta,\phi)\right|d\Omega\iint_{\Omega}\tilde{p}_{l,n}(\theta,\phi)\left|G_{m_j}(\theta,\phi)\right|d\Omega}} \tag{17}$$

has size $MN \times MN$ and the covariance matrix of the matrix channel of size $M \times M$ is combining the individual tap correlations describing the covariance between antennas over all taps.

III. EFFECTIVE CHANNEL GAIN

This section will provide the PDF and CDF of the effective channel gain. This is the channel gain after combining all branches (antenna elements and taps) at the BS. We focus on the matched filter for the single user case, since it is the optimal result for that specific user. Any other combination scheme under consideration of multiple users will provide poorer performance to the intended user. To leave no user in a multi-user setting behind, interference should be suppressed by other means than interference suppressing combining. The effective channel $\mathcal{H}$ for MRC is:

$$\mathcal{H} = \boldsymbol{w}^{\mathrm{T}}\boldsymbol{h} = \frac{\boldsymbol{h}^{\mathrm{H}}\boldsymbol{h}}{\sqrt{||\boldsymbol{h}||_2^2}} = \sqrt{\boldsymbol{h}^{\mathrm{H}}\boldsymbol{h}}, \tag{22}$$

and the corresponding effective channel power gain $\mathcal{Q}$:

$$\mathcal{Q} = |\mathcal{H}|^2 = \boldsymbol{h}^{\mathrm{H}}\boldsymbol{h} \tag{23}$$

is a CGQF of the channel vector and a coherent summation of all vector channel elements.

Closed-form approximations of the PDF and CDF of CGQFs are derived in the following. The general idea is based on the principles of the approximation of real Gaussian quadratic forms [20], but using the moment-generating function of the confluent non-central CGQF [21]. We have reformulated the recursion in the approximation to reduce the growth rate of some auxiliary variables. This allows to increase the approximation order, improving the accuracy of the method, enabling the analysis of LSAS. Furthermore, the local diversity [7] is approximated based on the PDF and CDF of the confluent CGQFs.

A. APPROXIMATIONS OF STATISTICS OF GAUSSIAN QUADRATIC FORMS

The vector $\boldsymbol{v} \sim \mathcal{CN}(\boldsymbol{\mu}, \boldsymbol{\Sigma})$ is an N-element random vector, with $\boldsymbol{\mu}$ and $\boldsymbol{\Sigma}$ characterizing the mean vector and positive definite covariance matrix of a multivariate complex normal distribution, respectively. The vector has a quadratic form $\mathcal{Q}$ with positive semidefinite operator matrix $\mathbf{A}$ being:

$$\mathcal{Q} = \boldsymbol{v}^{\mathrm{H}}\mathbf{A}\boldsymbol{v}. \tag{24}$$

This quadratic form has the same structure as the effective channel in (22), where $\boldsymbol{v} = \boldsymbol{h}$ and $\mathbf{A} = \mathbf{I}$.

The vector $\boldsymbol{v}$ can be decomposed:

$$\boldsymbol{v} = \mathbf{L}\boldsymbol{x} + \boldsymbol{\mu} = \mathbf{L}\big(\boldsymbol{x} + \tilde{\boldsymbol{\mu}}\big). \tag{25}$$

such that $\boldsymbol{x} \sim \mathcal{CN}_N(0, \mathbf{I})$ is an iid standard $\mathcal{CN}$-RV. The matrix $\mathbf{L}$ provides a mixing of the iid variables to introduce the correlation given by $\boldsymbol{\Sigma}$ (e.g., by Cholesky decomposition $\boldsymbol{\Sigma} = \mathbf{L}\mathbf{L}^{\mathrm{H}}$) and a transformation of the mean vector $\tilde{\boldsymbol{\mu}} = \mathbf{L}^{-1}\boldsymbol{\mu}$.

Rewriting the quadratic form with the decomposed vector $\boldsymbol{v}$ results in:

$$\mathcal{Q} = (\boldsymbol{x} + \tilde{\boldsymbol{\mu}})^{\mathrm{H}}\mathbf{L}^{\mathrm{H}}\mathbf{A}\mathbf{L}(\boldsymbol{x} + \tilde{\boldsymbol{\mu}}) \tag{26}$$

which can be expressed in terms of eigenvalues λ_i of $\mathbf{L}^{\mathrm{H}}\mathbf{A}\mathbf{L}$:

$$\mathcal{Q} = \sum_i^N \lambda_i (x_i + \tilde{\mu}_i)^*(x_i + \tilde{\mu}_i) = \sum_i^N \lambda_i |x_i + \tilde{\mu}_i|^2. \tag{27}$$

This reveals the structure of a sum of λ_i weighted non-central χ^2 variables ($|x_i + \tilde{\mu}_i|^2 \sim \chi_2'^2(|\tilde{\mu}_i|^2)$). We observe that *the effective channel gain of any correlated $\mathcal{CN}$-RV can be rewritten as a sum of weighted independent non-central χ^2 variables*, where the weights are related to the covariance matrix.

A closed-form moment-generating function exists for this structure [21]:

$$M_{\mathcal{Q}}(s) = \prod_{i=1}^{n} \exp\left(\frac{|\tilde{\mu}_i|^2\lambda_i s}{1 - \lambda_i s}\right)(1 - \lambda_i s)^{-1}, \tag{28}$$

but can not be used to derive closed-forms of the corresponding PDF and CDF. Nonetheless, using a slightly modified moment-generating function which converges for approximation order $m \to \infty$ to the intended CGQF [20] gives the following approximation for the PDF:

$$f_{\mathcal{Q}}(x) \approx M_{\mathcal{Q}}\left(\frac{1-m}{x}\right)\frac{(m-1)^m}{x^{m+1}(m-1)!}U_m\left(\frac{1-m}{x}\right), \tag{29}$$

as well as CDF

$$F_{\mathcal{Q}}(x) \approx M_{\mathcal{Q}}\left(\frac{1-m}{x}\right)\sum_{k=0}^{m-1}\frac{(m-1)^k}{x^k k!}U_k\left(\frac{1-m}{x}\right), \tag{30}$$

with auxiliary variables:

$$U_k(s) = \sum_{j=0}^{k-1}\binom{k-1}{j}V_{k-1-j}(s)U_j(s) \tag{31}$$

$$V_t(s) = t!\sum_{i=1}^{n}\lambda_i^{t+1}\frac{(t+1)|\tilde{\mu}_i|^2 - \lambda_i s + 1}{(1-\lambda_i s)^{t+2}}. \tag{32}$$

The variable $U_k(s)$ can be calculated by recursion and builds on $g_t(s)$. Both auxiliary variables grow fast and overflow a floating point number, when the approximation order m grows large. Detection of the overflow allows to gracefully identify the maximum approximation order, where results are still valid.

To improve the numerical properties of the approximation, we reformulate the auxiliary variables in (31) and (32). The growth rate can be reduced by redistributing the fast growing faculty terms $k!$ and $t!$ as follows:

$$\tilde{U}_k(s) = (-s)^k\frac{U_k(s)}{k!} \tag{33}$$

$$\tilde{V}_t(s) = (-s)^t\frac{V_{t-1}(s)}{(t-1)!}. \tag{34}$$

This eliminates the binomial in (31) and gives the modified auxiliary variables:

$$\tilde{U}_k(s) = \frac{1}{k}\sum_{j=0}^{k-1} \tilde{V}_{k-j}(s)\tilde{U}_j(s), \tag{35}$$

$$\tilde{V}_t(s) = (-s)^t \sum_{i}^{n} \lambda_i^t \frac{t|\tilde{\mu}_i|^2 - \lambda_i s + 1}{(1-\lambda_i s)^{t+1}}. \tag{36}$$

Additionally, the approximations of the PDF and CDF are simplified to:

$$f_{\mathcal{Q}}(x) \approx \frac{m}{x} M_Q\left(\frac{1-m}{x}\right)\tilde{U}_m\left(\frac{1-m}{x}\right), \tag{37}$$

$$F_{\mathcal{Q}}(x) \approx M_Q\left(\frac{1-m}{x}\right)\sum_{k=0}^{m-1}\tilde{U}_k\left(\frac{1-m}{x}\right). \tag{38}$$

and the local diversity $\mathcal{D}$ [7] of a quadratic form follows:

$$\mathcal{D}(x) = x\frac{f_{\mathcal{Q}}(x)}{F_{\mathcal{Q}}(x)} \approx m\frac{\tilde{U}_m\left(\frac{1-m}{x}\right)}{\sum_{k=0}^{m-1}\tilde{U}_k\left(\frac{1-m}{x}\right)}. \tag{39}$$

This form allows to calculate the local diversity as a byproduct of the PDF calculation.

IV. EXAMPLES OF SPATIAL CORRELATION

This section demonstrates the effect of different PAS, as well as antenna pattern, on the spatial correlation between antenna elements. We will show the differences to the classic case of isotropic antennas in Rayleigh fading.

The spatial correlation is completely described by the covariance matrix $\mathbf{\Sigma}$ and takes into account both, the PAS of the diffuse channel and the directivity of the antenna elements. Here, we only consider uncorrelated scattering for simplicity, but scenarios with correlation between multiple taps can be covered too. First, different PAS (see Fig. 2) for ULAs with omni-directional antenna elements are presented and their influence on the correlation coefficients is analyzed. Then, antenna element patterns are added into the consideration.

A. POWER ANGULAR SPECTRA

1) OMNI-DIRECTIONAL CHANNELS

The classic Rayleigh channel is omni-directional in two dimensions and has a uniform PAS in azimuth restricted to a single polar angle of $\phi = \pi/2$:

$$p(\theta,\phi) = \tilde{p}(\theta,\phi) = \frac{1}{2\pi}\delta\left(\phi - \frac{\pi}{2}\right). \tag{40}$$

However, a Rayleigh fading envelope does not necessarily require the diffuse component to be omni-directional. Evaluating the correlation coefficient for a uniformly spaced x-oriented ULA with Δd element spacing gives:

$$\rho_{i,j}^{\text{omni}} = \frac{\delta(n_i - n_j)}{2\pi}\int_0^{2\pi} \exp\left(\mathrm{j}2\pi\left(m_i - m_j\right)\frac{\Delta d}{\lambda}\cos\theta\right)d\theta \tag{41}$$

$$= \delta(n_i - n_j)J_0\left(2\pi\left(m_i - m_j\right)\frac{\Delta d}{\lambda}\right), \tag{42}$$

where the δ-function ensures uncorrelated taps and $J_0(\cdot)$ is the zero-order Bessel function of the first kind.

The Rice channel needs to account for the $\mathcal{K}$-factor in addition, but the correlation properties stay the same and $\rho_{i,j}^{\text{omni}}$ provides the correlation coefficient. The corresponding PAS, where the available channel power has been normalized, has the following PDF [22, Sec. 6.4.4]:

$$p(\theta,\phi) = \frac{1}{2\pi(\mathcal{K}+1)}\left[1 + 2\pi\mathcal{K}\delta(\theta - \bar{\theta})\right]\delta\left(\phi - \frac{\pi}{2}\right), \tag{43}$$

where the angle $\bar{\theta}$ defines the direction of the incoming wave responsible for the deterministic part of the channel.

2) SECTOR CHANNEL

It is more common in outdoor propagation scenarios with elevated BS, that the diffuse part is restricted to a sector with an opening angle ψ, We are continuing with two-dimensional propagation coming from the horizon and define the sector PAS as:

$$\tilde{p}(\theta,\phi) = \delta\left(\phi - \frac{\pi}{2}\right)\begin{cases}\frac{1}{\psi} & \text{with } \tilde{\theta}_0 - \frac{\psi}{2} \le \theta \le \tilde{\theta}_0 + \frac{\psi}{2} \\ 0 & \text{otherwise}\end{cases} \tag{44}$$

where $\tilde{\theta}_0$ is the directional centre of the diffuse part.

The correlation coefficient resulting from propagation from a uniform diffuse sector impinging on a ULA is

$$\rho_{i,j}^{\text{uni}} = \frac{\delta(n_i - n_j)}{\psi}\int_{\tilde{\theta}-\frac{\psi}{2}}^{\tilde{\theta}+\frac{\psi}{2}} \exp\left(\mathrm{j}2\pi\left(m_i - m_j\right)\frac{\Delta d}{\lambda}\cos\theta\right)d\theta. \tag{45}$$

This integral can be solved numerically.

A tapered sector model can be achieved with a von Mises distribution,[3] to avoid discontinuities in the PAS. The PDF for the diffuse channel PAS is:

$$\tilde{p}(\theta,\phi) = \delta(\phi)\frac{\exp\left(\kappa\cos\left(\theta - \tilde{\theta}_0\right)\right)}{2\pi I_0(\kappa)}, \tag{46}$$

where κ is a concentration measure. The correlation coefficient can be calculated by solving (17) numerically.

In Fig. 2 three different diffuse PAS are displayed. The corresponding correlation function for two omni-directional elements separated in x-direction are shown in Fig. 3. It is clear that the actual distribution of the PAS has a strong influence on the spatial correlation between antenna elements. The wider the sector of the diffuse component is, the slower is the decay of the correlation coefficient magnitude.

B. ANTENNA ELEMENT PATTERN

The actually observable diffuse part of the channel depends not only on the direction of the incoming diffuse waves, but on the antenna element pattern in addition. For simplicity, we are continuing with the specialization to two-dimensions.

3. The circular equivalent to the real Gaussian distribution.

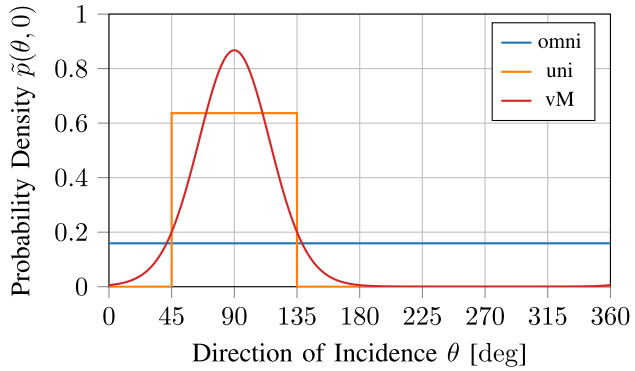

FIGURE 2. Power angular spectra for three different scenarios are shown, namely an omnidirectional channel (omni), an uniform sector channel (uni, $\alpha = 90°$, $\tilde{\theta}_0 = 90°$) and a von Mises channel (vM, $\kappa = 5$, $\tilde{\theta}_0 = 90°$).

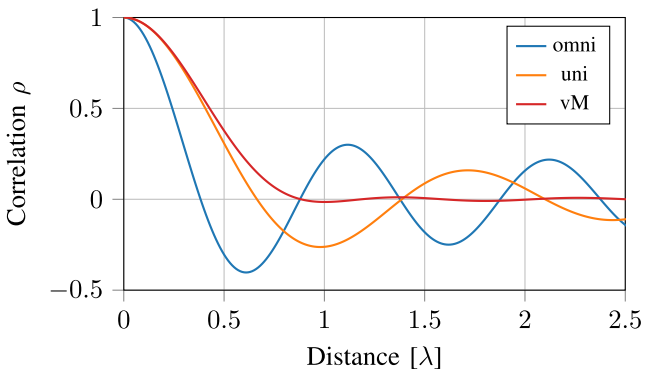

FIGURE 3. The correlation between two omni-directional antenna elements spaced at a distance in *x*-direction is shown for the three different PASs in Fig. 2.

The directivity D of each antenna element is described by the shape of the antenna pattern $F(\theta, \phi)$ and the maximum directivity D_0:

$$D(\theta, \phi) = D_0 F(\theta, \phi). \tag{47}$$

A generic uni-directional two-dimensional antenna pattern can be modeled as a cosine to the power of ζ [23], where θ_0 fixes the azimuth angle for D_0:

$$F(\theta, \phi) = \begin{cases} \cos^{\zeta}(\theta - \theta_0)\delta\left(\phi - \frac{\pi}{2}\right) & \theta_0 - \frac{\pi}{2} \leq \theta \leq \theta_0 + \frac{\pi}{2} \\ 0 & \text{elsewhere.} \end{cases} \tag{48}$$

The higher ζ is, the more directional the antenna pattern. The half power beam width can be derived by evaluating $F(\theta, \phi) = 1/2$:

$$\theta_{\text{HPBW}} = 2 \arccos\left(\sqrt[\zeta]{\frac{1}{2}}\right). \tag{49}$$

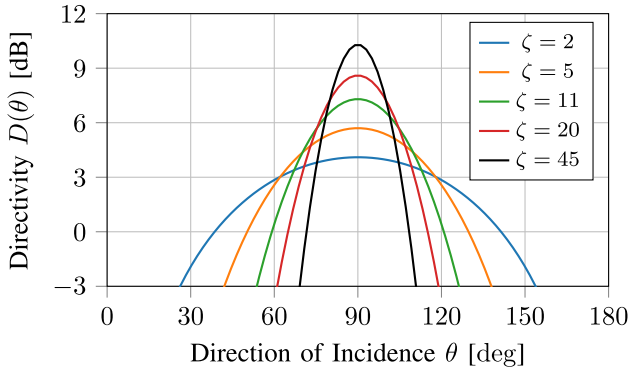

FIGURE 4. Directivity of the uni-directional generic $\cos^{\zeta}(\theta - \theta_0)$ antenna element for $\theta_0 = 90°$.

TABLE 1. Properties of the generic uni-directional $\cos^{\zeta}(\theta - \theta_0)$ antenna element.

ζ	0	2	5	11	20	45
D_0 [dB]	1.0	4.1	5.7	7.3	8.6	10.3
θ_{HPBW}	(180°)	90°	59°	40°	30°	20°

The maximum directivity with respect to an isotropic source can be evaluated by:

$$D_0 = \frac{4\pi}{\iint_{\Omega} F(\theta, \phi) d\Omega}. \tag{50}$$

The pattern for different ζ is shown in Fig. 4 and the maximum directivity and half power beam width are presented in Table 1.

The antenna gain in Section II is connected to the directivity via the antenna efficiency ϵ:

$$G(\theta, \phi) = \eta D(\theta, \phi) \tag{51}$$

For the generic $cos^{\zeta}(\theta - \theta_0)$, the correlation coefficient in (17) can be simplified as shown in (52), shown at the bottom of the page. Fig. 5 depicts the influence of the directivity of the antenna elements on the correlation coefficient at an element spacing of $\lambda/2$. The more directive the antenna elements are, the higher the correlation coefficient for ULAs (squint angle 0°). If the elements are squinting into different directions (e.g., if they are distributed over an arc), then the behaviour changes and the correlation falls off once both beams stop to overlap.

V. SIMULATIONS

In the following section, simulation results are presented, to verify the approximations due to the confluent CGQF. To illustrate the versatility of the method, we compare a ULA BS with a half-circle BS layout for antenna elements with varying directivity. This shall demonstrate how

$$\rho^{t}_{m_i,m_j} = \frac{D_0}{4\pi} \int_{\max\left(\theta_{0_i}-\frac{\pi}{2}, \theta_{0_j}-\frac{\pi}{2}\right)}^{\min\left(\theta_{0_i}+\frac{\pi}{2}, \theta_{0_j}+\frac{\pi}{2}\right)} \sqrt{\cos^{\zeta}\left(\theta - \theta_{0_i}\right) \cos^{\zeta}\left(\theta - \theta_{0_j}\right)} \exp\left(\mathrm{j}\Delta\varphi_{m_i,m_j}\left(\theta, \frac{\pi}{2}\right)\right) d\theta \tag{52}$$

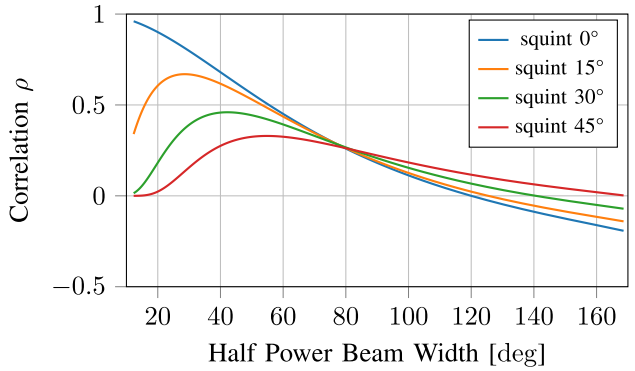

FIGURE 5. The correlation between two antenna elements spaced at a distance of 0.5 λ is shown for different squint angles.

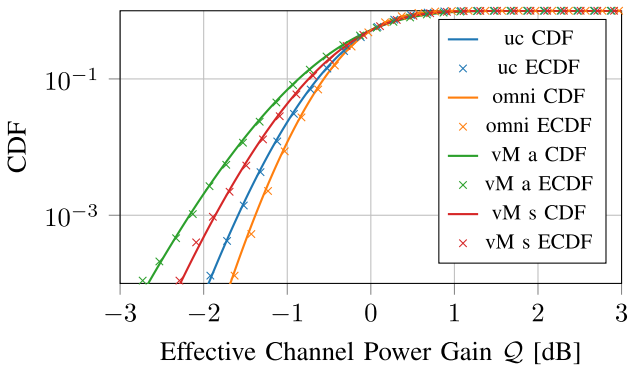

FIGURE 6. Verification of the cumulative distribution functions (CDFs) approximated by complex Gaussian quadratic forms for a 32 antenna element uniform linear array in a single tap fading environment with $\mathcal{K}$-factor 4. The empirical cumulative distribution functions (ECDF) are generated from simulation results. Four different power angular spectrum are evaluated: uncorrelated (uc), omni-directional (omni), von Mises aligned (vM a) and von Mises squinting (vM s). The approximations provide accurate results for the correlated and uncorrelated cases.

TABLE 2. Overview over simulated scenarios with power angular spectrum for uncorrelated (uc), omnidirectional (omni) and von Mises channels.

Scenario	Verification		Array Configurations
Array Layout	ULA		half circle & ULA
# of Antennas M	32		32
# of Taps N	1		1
Ant. Element ζ	0		2 & 5 & 20
PAS	uc & omni	von Mises	von Mises (aligned)
Rician Factor $\mathcal{K}$	0	4	0 & 4
Determ. Dir. $\bar{\theta}$		70°	30° & 60°
Concentration κ		5	5
Diffuse Dir. $\tilde{\theta}_0$		70° & 90°	30° & 60°

the introduced model allows a simple performance evaluation of correlated Rician radio channels under consideration of antenna element pattern, array layout and Rician fading channels. The different scenarios are summarized in Table 2.

A. VERIFICATION

To verify that the analytic approximations provide accurate results, a number of diffuse plane waves impinging on an ULA with isotropic antenna elements are simulated. The 32 antenna element ULA with $\lambda/2$ spacing in x-direction is situated in a single tap Rician fading environment with $\mathcal{K}$-factor 4 for four different PAS:

- uncorrelated
- omnidirectional diffuse scattering
- von Mises scattering aligned with deterministic component ($\kappa = 5, \bar{\theta} = \tilde{\theta}_0 = 70°$)
- von Mises scattering squinting with respect to the deterministic component ($\kappa = 5, \bar{\theta} = 70°, \tilde{\theta}_0 = 90°$).

The uncorrelated simulation adhering to (6) and (7) is generating independent plane waves for each antenna element, whilst the other three simulations have the same plane waves impinging on all elements. The empirical CDFs are based on 1×10^6 trials with 800 plane waves forming the diffuse channel according to the PAS.

These verification settings cover wide-band results up to a certain number of taps too, since both taps and antennas link to $\mathcal{CN}$-RV elements. The multi-antenna single-tap case allows for a fully populated correlation matrix in our uncorrelated scattering setting and is therefore more challenging than a single antenna 32 tap scenario.

The CDFs are shown in Fig. 6. Simulations and approximations give consistent results for all cases. It is important to note, that uncorrelated antenna elements do *not* in general provide the best results once the channel shows Rician fading. It depends on the superposition of the phases that the deterministic and diffuse component cause on the antenna elements. A certain correlation between close antenna elements improves the situation if the diffuse component is orthogonal to the deterministic component. This reduces the probability that the diffuse component acts destructively on the deterministic component, since they align over close antenna elements. This effect is visible both, in comparison with the uncorrelated and omni-directional PAS and for the aligned and squinting von Mises scattering. Nonetheless, for real scenarios it is highly probable the deterministic and the diffuse component are aligned (e.g., von Mises aligned case), leading to a loss of performance over the uncorrelated case.

The corresponding local diversity is presented in Fig. 7. The classic diversity would be 32 for a BS with 32 uncorrelated antenna elements. The local diversity at interesting outage probabilities is heavily depending on the PAS of the diffuse component. Additionally, it is not predictable from the number of array elements only [7].

B. ARRAY CONFIGURATIONS

Here, we want to analyse the implications of two different BS array configurations in aligned von Mises scattering from different angles with $\mathcal{K}$-factors zero and 4. An ULA is the reference configuration, since it is used abundantly for theoretical discussions due to its mathematical tractability. Equipped with directional antenna elements it could model a BS mounted to a building edge fairly well. As alternative,

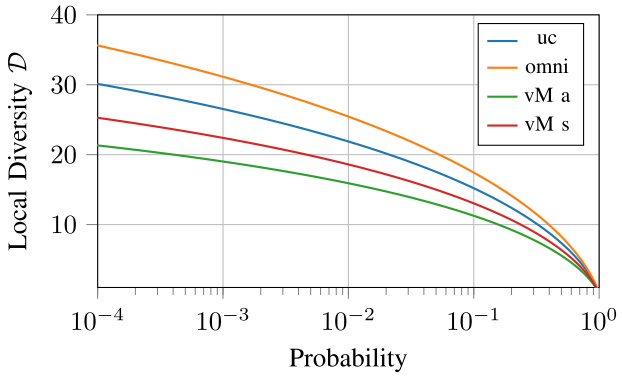

FIGURE 7. The local diversity approximated by complex Gaussian quadratic forms for a 32 antenna element uniform linear array in a single tap fading environment with isotropic antenna pattern is shown for the four verification scenarios in Fig. 6.

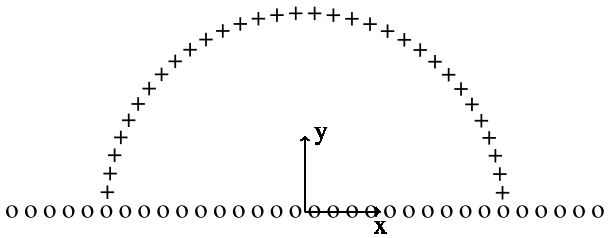

FIGURE 8. Array configuration of the ULA (o) and half circle array (+).

the elements will be distributed over a half circle to reduce the extent in one direction, whilst increasing it into the other. Hence, with the same directional elements, a wider sector will be illuminated more evenly, reducing the maximum gain into broadside direction. Both configurations are sketched in Fig. 8.

Fig. 9 shows results for different von Mises PASs. Solid lines and dashed lines indicate the ULA and half circle BS layout, respectively. In general, high directivity of the antenna elements is not giving advantages in the considered cases. The reason is that the main direction of the elements has to match the direction of the incoming waves, but it is not steerable. The penalty for higher gain elements is lower in the half circle arrangement, since at least a few antennas are pointing towards a possible user.

For the low directivity elements, a deterministic channel component can be used efficiently, since the array factor allows coherent combination. In the high directivity case, at least one element needs to be aligned. The more a user is received towards the end-fire direction of the ULA, the better is the half circle configuration in comparison. Eventually, the half circle BS provides a more evenly distributed coverage and is less sensitive to the direction of the incoming waves. Furthermore, in multi-user applications, different users are more likely to have stronger contributions to different antenna element subsets of the half circle array.

Fig. 10 presents the local diversities for the two BS under different fading conditions. Only the low directivity case ($\zeta = 2$) has been taken into account, to allow for visual comparison of the influence of different PASs. Both, uncorrelated Rayleigh and Rician fading provide more local diversity than their counterparts with constricted PAS. The half circle BS has always less local diversity in comparison to the ULA BS. This is due to fewer antenna elements being illuminated by the diffuse component, that provides spatial diversity. A higher $\mathcal{K}$-factor provides a higher local diversity for all cases, since it becomes more unlikely that the diffuse component of the channel cancels the deterministic component out.

VI. DISCUSSION

The proposed correlated Rician model increases the realism and complexity of a massive MIMO BS propagation analysis over simpler uncorrelated models. Additionally, antenna array geometry, antenna element orientation and PASs have been accounted for to determine the covariance matrix of the $\mathcal{CN}$-RV, allowing for evaluation of different BS designs for a given scenario. The parameters of the $\mathcal{CN}$-RV can alternatively be based on the simplified 3rd Generation Partnership Project Urban Microcell model as described in [5] and our CGQFs approach still gives the PDF and CDF of the effective channel. Furthermore, the method can be generalized to handle, e.g., power variation between antenna elements through the operator matrix.

Covariance is sometimes elusive and hard to measure properly in the field. However, by inspection of the quadratic form in (27), it is clear, that the properties of the eigenvalues of the covariance matrix are of central relevance to capture the effect of correlation on the effective channel. Moreover, considering *universality* in random matrix theory [24], the distribution of eigenvalues behaves asymptotically as if the matrix elements are Gaussian distributed. Therefore, the CGQF results are less sensitive to the actual individual correlation coefficients.

So far, we only demonstrated over-the-horizon propagation with the example PASs. Nonetheless, the described framework allows for three-dimensional considerations. The impact of incoming waves from different elevation angles depends obviously on the weighting imposed by antenna element pattern and array geometry. In general, additional local diversity is available, but the BS design needs to take this into account to benefit from it. The proposed model is flexible enough to allow BS performance comparisons for a combination of surface and aerial users.

VII. CONCLUSION

A thorough way of handling correlated Rician fading for LSASs has been presented. The accurate approximations can be used to analyse the effective channel of massive MIMO BSs. The framework allows consideration of inter-tap correlation in addition to the outlined antenna correlations. Inter-tap correlation can occur, e.g., if distributed antenna arrays are spaced further apart than the distance related to the duration of a single tap.

The provided correlated $\mathcal{CN}$-RV channel model is general and the $\mathcal{K}$-factor parameterizations allows investigation of Rician and Rayleigh fading at each antenna and

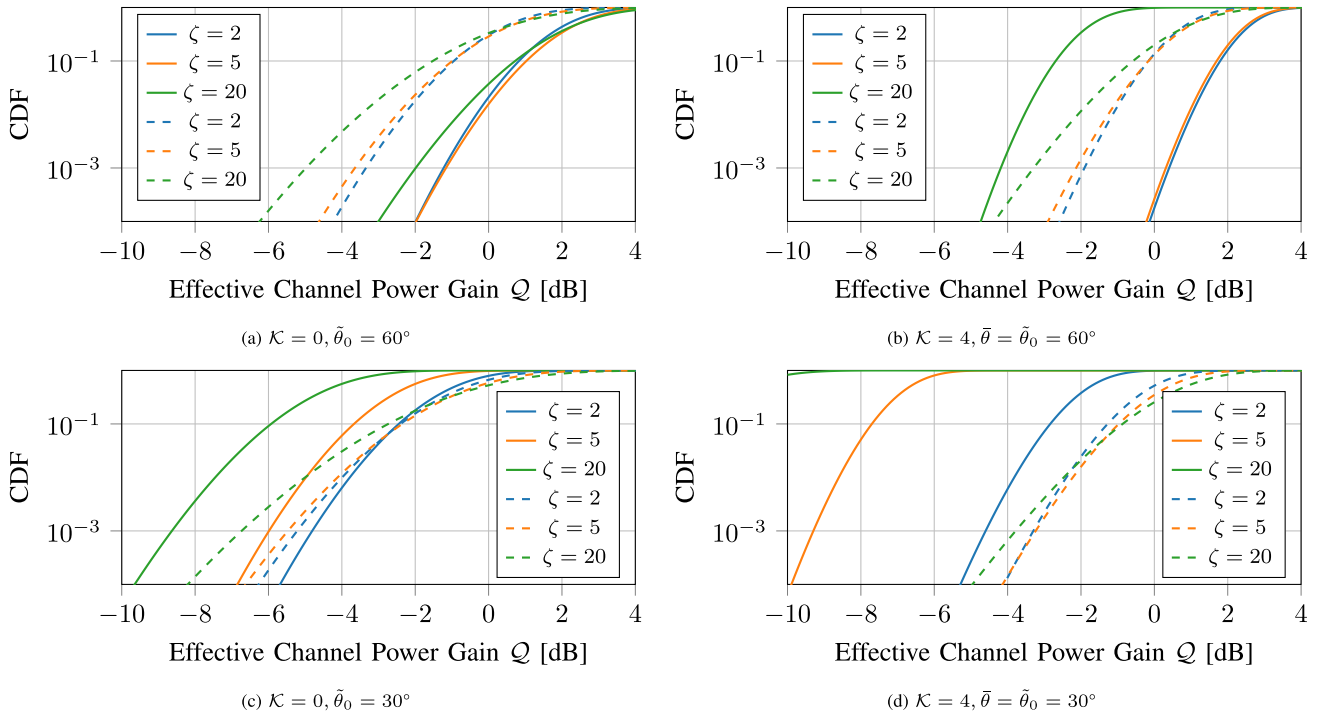

(a) $\mathcal{K} = 0, \tilde{\theta}_0 = 60°$ (b) $\mathcal{K} = 4, \bar{\theta} = \tilde{\theta}_0 = 60°$

(c) $\mathcal{K} = 0, \tilde{\theta}_0 = 30°$ (d) $\mathcal{K} = 4, \bar{\theta} = \tilde{\theta}_0 = 30°$

FIGURE 9. The plots show the effective channel for different directivities (colors), power angular spectrums with concentration $\kappa = 5$ of a uniform linear array (ULA) (solid lines), and half circle array (dashed lines). The ULA performance is more dependent on broadside incidence of the waves, than the half circle array, especially for higher directivity elements. In all shown scenarios (parameters given below the subfigures) is lower directivity more beneficial and the half circle arrangement trades peak directivity towards broadside with increased directivity towards the end-fire direction of the ULA.

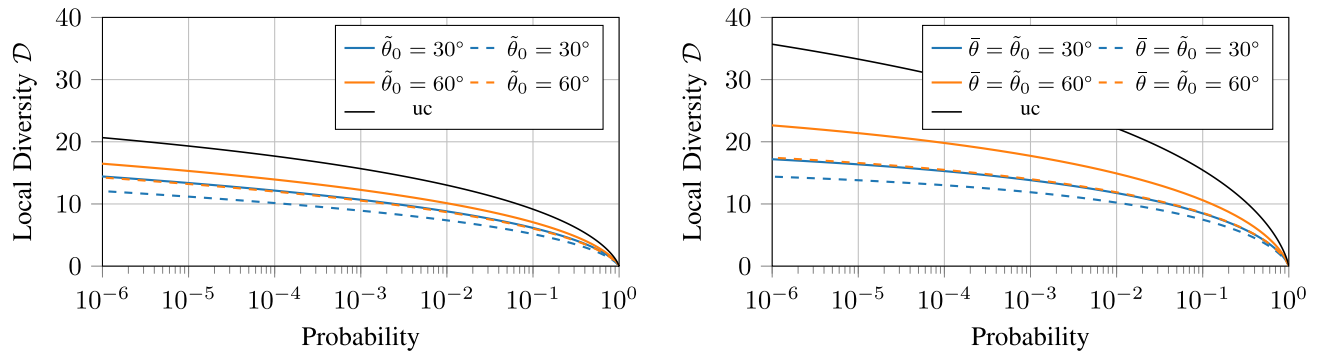

(a) $\mathcal{K} = 0$ (b) $\mathcal{K} = 4$

FIGURE 10. Local diversities are shown for the uniform linear array (solid line) and half circle (dashed line) base station with low directivity elements ($\zeta = 2$). The different colours correspond to different von Mises power angular spectrum with parameters given in the legend for two different $\mathcal{K}$-factors. In general, the half circle BS has less local diversity at a certain outage probability. Moreover, a higher $\mathcal{K}$-factor gives higher local diversity. All constricted cases of diffuse scattering provide less local diversity than the uncorrelated (uc) Rayleigh/Rice (solid black) channel.

delay tap with arbitrary correlation coefficients. Correlation coefficients have been related to the PAS of the diffuse channel component and consider the antenna element pattern in addition. A plane wave model provides the foundation of the complex normal element statistics and the tractability of correlation coefficients. To capture near-field aspects that become more prominent for larger apertures, future research should investigate the differences that a spherical wave model would introduce.

Low-directivity antenna elements provide better overall system performance than high-directivity elements, once the BS grows to a reasonable size. This is mainly caused by being less prone to the direction of incoming waves, because the main gain is coming from the steerable array factor and not the static element factor. Arranging the elements in a half-circle illuminates a region more evenly than a ULA, but reduces the peak gain for broad-side radiation. Moreover, the local diversity is reduced for the half-circle BS and a directional diffuse part since fewer elements pick up significant energy, even though they are less correlated. A thorough analysis of the system performance would, in addition to the presented channel properties, need to include hardware imperfections like phase noise and timing jitter.

The complete statistic of the effective channel gain for correlated Rician fading channels is described through the provided PDF or CDF. This allows the investigation of instantaneous metrics of the single user performance beyond the mean and variance of the combined received signal.

REFERENCES

[1] E. Björnson, L. Sanguinetti, H. Wymeersch, J. Hoydis, and T. L. Marzetta, "Massive MIMO is a reality—What is next? Five promising research directions for antenna arrays," *Digital Signal Process.*, vol. 94, pp. 3–20, Nov. 2019.

[2] D. Ciuonzo, P. S. Rossi, and S. Dey, "Massive MIMO channel-aware decision fusion," *IEEE Trans. Signal Process.*, vol. 63, no. 3, pp. 604–619, Feb. 2015.

[3] A.-S. Bana *et al.*, "Massive MIMO for Internet of Things (IoT) connectivity," *Phys. Commun.*, vol. 37, Dec. 2019, Art. no. 100859.

[4] Ö. Özdogan, E. Björnson, and E. G. Larsson, "Massive MIMO with spatially correlated Rician fading channels," *IEEE Trans. Commun.*, vol. 67, no. 5, pp. 3234–3250, May 2019.

[5] A. Á. Polegre, F. Riera-Palou, G. Femenias, and A. G. Armada, "Channel hardening in cell-free and user-centric massive MIMO networks with spatially correlated Ricean fading," *IEEE Access*, vol. 8, pp. 139827–139845, 2020.

[6] Z. Wang, J. Zhang, E. Björnson, and B. Ai, "Uplink performance of cell-free massive MIMO over spatially correlated Rician fading channels," *IEEE Commun. Lett.*, vol. 25, no. 4, pp. 1348–1352, Apr. 2021.

[7] J. Abraham and T. Ekman, "Local diversity and ultra-reliable antenna arrays," Nov. 2021, *arXiv: 2108.00712*.

[8] Y. Chen and C. Tellambura, "Distribution functions of selection combiner output in equally correlated Rayleigh, Rician, and Nakagami-m fading channels," *IEEE Trans. Commun.*, vol. 52, no. 11, pp. 1948–1956, Nov. 2004.

[9] M. Chiani, M. Win, and A. Zanella, "On the capacity of spatially correlated MIMO Rayleigh-fading channels," *IEEE Trans. Inf. Theory*, vol. 49, no. 10, pp. 2363–2371, Oct. 2003.

[10] R. U. Nabar, H. Bolcskei, and A. J. Paulraj, "Diversity and outage performance in space-time block coded Ricean MIMO channels," *IEEE Trans. Wireless Commun.*, vol. 4, no. 5, pp. 2519–2532, Sep. 2005.

[11] H. T. Hui, "The performance of the maximum ratio combining method in correlated rician-fading channels for antenna-diversity signal combining," *IEEE Trans. Antennas Propag.*, vol. 53, no. 3, pp. 958–964, Mar. 2005.

[12] K. A. Hamdi, "Capacity of MRC on correlated Rician Fading channels," *IEEE Trans. Commun.*, vol. 56, no. 5, pp. 708–711, May 2008.

[13] L. Sanguinetti, A. Kammoun, and M. Debbah, "Theoretical performance limits of massive MIMO With uncorrelated Rician fading channels," *IEEE Trans. Commun.*, vol. 67, no. 3, pp. 1939–1955, Mar. 2019.

[14] M. Matthaiou, H. Q. Ngo, P. J. Smith, H. Tataria, and S. Jin, "Massive MIMO with a generalized channel model: Fundamental aspects," in *Proc. IEEE 20th Int. Workshop Signal Process. Adv. Wireless Commun. (SPAWC)*, 2019, pp. 1–5.

[15] S. Loyka and J. Mosig, "Channel capacity of N-antenna BLAST architecture," *Electron. Lett.*, vol. 36, no. 7, pp. 660–661, 2000.

[16] S. L. Loyka, "Channel capacity of MIMO architecture using the exponential correlation matrix," *IEEE Commun. Lett.*, vol. 5, no. 9, pp. 369–371, Sep. 2001.

[17] W. A. Al-Hussaibi, "A generalised antenna correlation model for accurate performance evaluation of 2D massive MIMO communication systems," *Aust. J. Electr. Electron. Eng.*, vol. 17, no. 4, pp. 269–277, 2020.

[18] E. Björnson, J. Hoydis, and L. Sanguinetti, "Massive MIMO networks: Spectral, energy, and hardware efficiency," *Found. Trends Signal Process.*, vol. 11, nos. 3–4, pp. 154–655, 2017.

[19] G. Ghiaasi, J. Abraham, E. Eide, and T. Ekman, "Effective channel hardening in an indoor multiband scenario," *Int. J. Wireless Inf. Netw.*, vol. 26, no. 4, pp. 259–271, Jul. 2019.

[20] P. Ramírez-Espinosa, D. Morales-Jimenez, J. A. Cortés, J. F. Paris, and E. Martos-Naya, "New approximation to distribution of positive RVs applied to Gaussian quadratic forms," *IEEE Signal Process. Lett.*, vol. 26, no. 6, pp. 923–927, Jun. 2019.

[21] P. Ramírez-Espinosa, L. Moreno-Pozas, J. F. Paris, J. A. Cortés, and E. Martos-Naya, "A new approach to the statistical analysis of non-central complex Gaussian quadratic forms with applications," *IEEE Trans. Veh. Technol.*, vol. 68, no. 7, pp. 6734–6746, Jul. 2019.

[22] G. D. Durgin, *Space-Time Wireless Channels* (Prentice Hall Communications Engineering and Emerging Technologies Series). Upper Saddle River, NJ, USA: Prentice Hall, 2002.

[23] C. A. Balanis, *Antenna Theory: Analysis and Design*, 4th ed. Hoboken, NJ, USA: Wiley, 2016.

[24] A. Edelman, A. Guionnet, and S. Péché, "Beyond universality in random matrix theory," *Ann. Appl. Probab.*, vol. 26, no. 3, pp. 1659–1697, 2016.

JENS ABRAHAM (Graduate Student Member, IEEE) received the Dipl.-Ing. degree in electrical engineering from TU Dresden, Dresden, Germany, in 2015. He is currently pursuing the Ph.D. degree with the Department of Electronics, Norwegian University of Science and Technology, Trondheim, Norway. From 2015 to 2017, he was a Research Assistant with the Astrophysics Group, Cavendish Laboratory, University of Cambridge, Cambridge, U.K. His current research interests include measurements and modeling of massive MIMO radio channels.

PABLO RAMÍREZ-ESPINOSA received the M.Sc. and Ph.D. degrees in telecommunication engineering from the University of Málaga, Spain, in 2017 and 2020, respectively. From 2017 to 2020, he was an Assistant Researcher with the Communication Engineering Department, University of Málaga. In March 2020, he joined the Connectivity Section, Electronic Systems Department, Aalborg University, where he is currently a Postdoctoral Researcher. He has been a Visiting Researcher with the Queen's University of Belfast in 2018. His main research activities are in wireless communications, particularly massive MIMO, dynamic metasurfaces antennas, ultra-reliable low-latency communications, channel modeling, and physical-layer security, as well as applied statistics. From 2019 to 2020, he received the IEEE TRANSACTIONS ON COMMUNICATIONS Exemplary Reviewer Certificate.

TORBJÖRN EKMAN (Member, IEEE) was born in Huddunge, Sweden, in 1969. He received the M.Sc. degree in engineering physics and the Ph.D. degree in signal processing from Uppsala University, Sweden, in 1994 and 2002, respectively. From 2002 to 2005, he made his postdoctoral studies with UniK, Kjeller, Norway. From 1997 to 1998, he was a Visiting Scientist with the Institute of Communications and Radio-Frequency Engineering, TU Wien, Austria, on a Marie Curie Grant. From 1999 to 2002, he was visiting the Digital Signal Processing Group, University of Oslo, Norway. In 2006, he joined the Norwegian University of Science and Technology, Trondheim, Norway, where he is a Professor with the Department of Electronic Systems. He is currently participating in projects on micro satellites, autonomous ships, and costal and arctic maritime operations. His current research interests include signal processing in wireless communications, micro satellite communication, massive MIMO, and dynamic radio channel modeling.